Numerical analysis of effective models for flux-tunable transmon systems

H. Lagemann,[1,2] D. Willsch,[1] M. Willsch,[1] F. Jin,[1] H. De Raedt,[1,3] and K. Michielsen[1,2]

[1] *Institute for Advanced Simulation, Jülich Supercomputing Centre, Forschungszentrum Jülich, D-52425 Jülich, Germany*

[2] *RWTH Aachen University, D-52056 Aachen, Germany*

[3] *Zernike Institute for Advanced Materials, University of Groningen, Nijenborgh 4, NL-9747 AG Groningen, The Netherlands*

(Dated: January 10, 2022)

Simulations and analytical calculations that aim to describe flux-tunable transmons are usually based on effective models of the corresponding lumped-element model. However, when a control pulse is applied, in most cases it is not known how much the predictions made with the effective models deviate from the predictions made with the original lumped-element model. In this work we compare the numerical solutions of the time-dependent Schrödinger equation for both the effective and the lumped-element models, for various control pulses. We consider three different systems: a single flux-tunable transmon and two two-qubit systems. We find that a series of commonly applied approximations (individually and/or in combination) can change the response of a system substantially, when a control pulse is applied.

Keywords: Quantum Computation, Quantum Theory, Mesoscale and Nanoscale Physics, Superconductivity, Flux-tunable Transmons

I. INTRODUCTION

The successful construction of a fully functioning universal quantum computer comes with the promise of allowing us to solve certain computational problems faster (potentially exponentially faster) than with a classical computer. However, the construction of a universal quantum computer comes with its own challenges, i.e. the task to understand the dynamic behaviour of quantum systems.

Many experimental prototypes, which aim to realise a universal quantum computer, are based on superconducting circuits. Theoretical descriptions of these systems often use a so-called circuit Hamiltonian model. Here we make a lumped-element approximation [1, 2] to derive a Hamiltonian, see for example Ref. [3], which approximately describes the behaviour of a particular superconducting circuit.

Unfortunately, it is usually the case that the circuit Hamiltonian model is still too complicated to be treated analytically. Therefore, in most cases additional simplifications are made so that an approximant of the circuit Hamiltonian can be derived. These approximants usually do not come with an estimation of the corresponding approximation error.

In this work we numerically study several instances of such approximants, i.e. effective Hamiltonians, by comparing them to their circuit Hamiltonian counterparts. To this end, we solve the time-dependent Schrödinger equation (TDSE) for both models. This allows us to compare the corresponding solutions and to filter out differences. Furthermore, we also compare the spectra of selected models.

Since the number of different superconducting circuits is vast, we will focus on three different circuit Hamiltonians (two of them correspond to experimental systems; see Refs. [4, 5])) and their corresponding effective Hamiltonians. Note that for a particular circuit Hamiltonian there might exist a vast amount of different effective models.

Broadly speaking (here we neglect all systems which are not based on transmon qubits), one might divide the different circuit architectures into two categories: architectures which only use fixed-frequency transmon qubits (an architecture which is primarily studied by IBM) and those using flux-tunable transmon qubits to implement their two-qubit gates. In this work, we focus on circuits which use flux-tunable transmons to implement two-qubit gates. Additionally, we restrict our analysis to systems which only contain one or two qubits, as this suffices to show where the models deviate from each other.

We look at three different systems. The first system is a single flux-tunable transmon. The second system (architecture I) consists of two fixed-frequency transmons, coupled to a flux-tunable transmon (this transmon works as a coupler). The third system (architecture II) is made up of two flux-tunable transmons, coupled to a transmission line resonator (this resonator functions only as a coupler element).

This work is structured as follows. In Sec. II we introduce and define the different models (the circuit model Hamiltonians and their effective counterparts). Here we also define a simple control pulse. This pulse enables us to activate a variety of transitions between the states of the systems we consider. Section III introduces the simulation algorithm and its features. Section IV contains the main results of this work. First, in Sec. IV A, we study a single isolated flux-tunable transmon and analyse the validity of the approximations which lead to this effective model. Next, in Sec. IV B, we identify several transitions (interactions) which are suppressed by the approximations we make to derive the effective model. Finally, in Sec. IV C, we study two-qubit gate transitions, i.e. transitions which can be used to implement two-qubit gates (in the corresponding architectures I and II). Here we fo-

cus on the often made approximation (see Ref. [4, 6–9]) that the effective interaction strength is of static nature. A summary and conclusions drawn from our analysis are presented in Sec. V.

II. MODEL

In this section we introduce the circuit Hamiltonian model (see Sec. II A) and we review some commonly made arguments which justify the use of effective model Hamiltonians (see Sec. II B). Furthermore, in Sec. II C we define a control pulse which can be used to implement single- and two-qubit gate transitions.

A. Circuit Hamiltonians

The systems we intend to model in this work consist of two different types of transmons as well as transmission line resonators. The couplings between the different subsystems are modelled as dipole-dipole interactions.

The circuit Hamiltonian which describes the so-called fixed-frequency transmon [10] is defined as

$$\hat{H}_{\mathrm{Fix}} = E_C(\hat{n} - n_g(t))^2 - E_J\cos(\hat{\varphi}), \tag{1}$$

where E_C denotes the capacitive energy and E_J is the Josephson energy. The Hamiltonian is defined in terms of the charge ($\hat{n}$) and the flux ($\hat{\varphi}$) operators. The time-dependent variable $n_g(t)$ denotes a control field, which is related to the voltage pulse applied to the system.

The other type of transmon is the flux-tunable transmon [11]. This type of transmon is the main object of our investigation. The corresponding circuit Hamiltonian is defined as

$$\hat{H}_{\mathrm{Tun}} = E_C\hat{n}^2 - E_{J,1}\cos(\hat{\varphi}) - E_{J,2}\cos(\hat{\varphi} - \varphi(t)). \tag{2}$$

This system is characterised by two Josephson energies $E_{J,1}$ and $E_{J,2}$ and another time-dependent variable $\varphi(t)$, which represents an external flux. This external flux is dimensionless

$$\varphi(t) = \Phi(t)/\phi_0, \tag{3}$$

where $\Phi(t)$ has the dimension of flux and ϕ_0 is the flux quantum. Furthermore, since the Hamiltonian is 2π periodic, $\varphi(t)$ is usually given in units of 2π. We adopt this convention too.

Individual transmons can be coupled directly, or indirectly, or both. In this paper, we only consider indirect couplings. This means interactions between individual transmons are conveyed by an additional circuit element, often called a coupler. This coupler can be a transmon itself or a transmission line resonator.

Transmission line resonators are described by the Hamiltonian

$$\hat{H}_{\mathrm{Res}} = \omega^R\hat{a}^\dagger\hat{a}, \tag{4}$$

where ω^R is the resonator frequency. The operators $\hat{a}^\dagger$ and $\hat{a}$ are bosonic creation and annihilation operators.

We describe the dipole-dipole coupling between two arbitrary transmons i and j by means of the interaction operator

$$\hat{V}_{i,j} = G_{i,j}\hat{n}_i\hat{n}_j, \tag{5}$$

where $G_{i,j}$ is the interaction strength. Similarly, we model the coupling between an arbitrary resonator j and an arbitrary transmon i with the operator

$$\hat{W}_{j,i} = G_{j,i}(\hat{a}^\dagger + \hat{a})_j\hat{n}_i. \tag{6}$$

We can use the different subsystems and the corresponding interaction terms to construct different circuit architectures. In this work, we consider two different architectures, which use flux-tunable transmons to implement the Iswap and Cz two-qubit gates. Architecture I, which is discussed in Refs. [4, 8, 9, 12], is described by the circuit Hamiltonian

$$\hat{H}_I = \hat{H}_{\mathrm{Tun},2} + \hat{H}_{\mathrm{Fix},1} + \hat{H}_{\mathrm{Fix},0} + \hat{V}_{2,1} + \hat{V}_{2,0}, \tag{7}$$

and architecture II, which is discussed in Refs. [5, 13], is described by

$$\hat{H}_{II} = H_{\mathrm{Res},2} + \hat{H}_{\mathrm{Tun},1} + \hat{H}_{\mathrm{Tun},0} + \hat{W}_{2,1} + \hat{W}_{2,0}. \tag{8}$$

In the first case, we use a flux-tunable transmon to indirectly couple two fixed-frequency transmons. In the second case, we use a resonator as a coupler between two flux-tunable transmons. The device parameters that we use in our simulations to obtain the results in Sec. IV, are listed in Table I (for architecture I) and Table II (for architecture II), respectively.

B. Effective Hamiltonians

Circuit Hamiltonian Eq. (1) was analytically discussed by Koch et al. [10]. This work motivated several studies [4, 6–8, 14] where transmons (fixed-frequency and/or flux-tunable) are modelled as anharmonic oscillators with fixed or tunable frequencies. The anharmonic oscillator is defined in terms of the harmonic basis

$$\mathcal{B} = \{|m\rangle\}_{m\in\mathbb{N}}, \tag{9}$$

where $|m\rangle$ is an energy eigenstate of the harmonic oscillator Hamiltonian. The fixed-frequency transmon is modelled by means of the effective Hamiltonian

$$\hat{H}_{\mathrm{fix}} = \hat{H}^0_{\mathrm{fix}} + \hat{V}_{\mathrm{fix}}(t). \tag{10}$$

Here, the system is operated in the transmon regime with $E_J/E_C \gg 1$. The time-independent part $\hat{H}^0_{\mathrm{fix}}$ can be expressed in terms of projectors as

$$\hat{H}^0_{\mathrm{fix}} = \sum_{m=0,1,2,3}\left(m\omega + \frac{\alpha}{2}m(m-1)\right)|m\rangle\langle m|, \tag{11}$$

TABLE I. Device parameters for a tunable coupler architecture (architecture I). The parameter $\omega = E_1 - E_0$ denotes the qubit frequency and $\alpha = (E_2 - E_1) - (E_1 - E_0)$ is the so-called qubit anharmonicity. All units are in GHz except the flux offset parameter $\varphi_0 = \varphi(0)$ which is given in units of the flux quantum ϕ_0, see Eqs. (3) and (23). These parameters are motivated by experiments performed by Ganzhorn et al. [4].

i	$\omega/2\pi$	$\alpha/2\pi$	E_C	$E_{J,1}$	$E_{J,2}$	$\varphi_0/2\pi$	$G_{2,i}$
0	5.100	-0.310	6.777	84.482	n/a	n/a	0.085
1	6.200	-0.285	6.453	127.992	n/a	n/a	0.085
2	8.100	-0.235	5.529	112.450	134.999	0.15	n/a

TABLE II. Device parameters for architecture II. The parameters in this table have the same units as the parameters in Table I. These device parameters are motivated by experiments performed by Lacroix et al. [5].

i	$\omega^R/2\pi$	$\omega/2\pi$	$\alpha/2\pi$	E_C	$E_{J,1}$	$E_{J,2}$	$\varphi_0/2\pi$	$G_{2,i}$
0	n/a	4.200	-0.320	6.712	19.728	59.184	0	0.300
1	n/a	5.200	-0.295	6.512	30.265	60.529	0	0.300
2	45.000	n/a	n/a	n/a	n/a	n/a	n/a	n/a

where $\omega = E_1 - E_0 \simeq \sqrt{2E_C E_J}$ denotes the qubit frequency and $\alpha = (E_2 - E_1) - (E_1 - E_0) \simeq -E_C/4$ is the anharmonicity. Note that we truncate the complete state space, i.e. we only use the lowest four states to model the system.

The time-dependent term $\hat{V}_{\text{fix}}(t)$ allows us to influence the time evolution of the transmon. This term can be expressed as

$$\hat{V}_{\text{fix}}(t) = \Omega(t) \sum_{m=0,1,2,3} \sqrt{m+1}\,(|m\rangle\langle m+1| + |m+1\rangle\langle m|)\,, \tag{12}$$

where $\Omega(t) = -n_g(t)\sqrt{8E_C E_J}$.

Often the effective Hamiltonian for the flux-tunable transmon is defined in a similar way. Here one makes use of the similarity between both circuit Hamiltonians in Eqs. (1) and (2). We can make this similarity more explicit by recasting Eq. (2). The result reads

$$\hat{H}_{\text{Tun}} = E_C \hat{n}^2 - E_{J,\text{eff}}(t)\cos(\hat{\varphi} - \varphi_{\text{eff}}(t)), \tag{13}$$

with the effective Josephson energy

$$E_{J,\text{eff}}(t) = E_\Sigma \sqrt{\cos\left(\frac{\varphi(t)}{2}\right)^2 + d^2 \sin\left(\frac{\varphi(t)}{2}\right)^2}, \tag{14}$$

and the effective external flux

$$\varphi_{\text{eff}}(t) = \arctan\left(d \tan\left(\frac{\varphi(t)}{2}\right)\right). \tag{15}$$

Here, we introduced the new parameters $E_\Sigma = (E_{J,1} + E_{J,2})$ and $d = (E_{J,2} - E_{J,1})/(E_{J,2} + E_{J,1})$. The latter one is usually referred to as the asymmetry factor, see Ref. [7, 10].

Since both Hamiltonians in Eqs. (1) and (13) have the same form, it is usually argued, see Refs.[4, 6–9], that only the Josephson energy E_J in the expression for the qubit frequency $\omega \simeq \sqrt{2E_C E_J}$ has to be replaced by the effective Josephson energy $E_{J,\text{eff}}$. This leads then to the time-dependent qubit frequency

$$\omega(t) = \sqrt{2E_C E_\Sigma} \sqrt[4]{\cos\left(\frac{\varphi(t)}{2}\right)^2 + d^2 \sin\left(\frac{\varphi(t)}{2}\right)^2}. \tag{16}$$

Therefore the effective Hamiltonian reads

$$\hat{H}_{\text{tun}} = \sum_{m=0,1,2} \left(m\omega(t) + \frac{\alpha}{2} m(m-1)\right) |m\rangle\langle m|\,. \tag{17}$$

Since the model Hamiltonian for the transmission line resonator Eq. (4) is already diagonal, no further approximations are necessary. However, if we intend to derive effective Hamiltonians for the circuit Hamiltonians in Eqs. (7) and (8), we also have to consider the interaction operators. This means we have to replace the charge operator $\hat{n}$ by an effective operator $\hat{n}_{\text{eff}}$. In this work we use the operator

$$\hat{n}_{\text{eff}} = \sqrt[4]{\frac{E_J}{8E_C}} \sum_{m=0,1,2} \sqrt{m+1}\,(|m\rangle\langle m+1| + |m+1\rangle\langle m|)\,, \tag{18}$$

which was also discussed by Koch et al. [10]. If we couple flux-tunable transmons, we have to perform the substitution $E_J \to E_{J\text{eff}}(t)$. The effective interaction strength for a coupling between a fixed-frequency transmon i and a flux-tunable transmon j is given by

$$g_{j,i}(t) = G_{j,i} \sqrt[4]{\frac{E_{J_j\text{eff}}(t)}{8E_{C_j}}} \sqrt[4]{\frac{E_{J_i}}{8E_{C_i}}}, \tag{19}$$

where $G_{j,i}$ is the original coupling strength (see Eqs. (5) and (6)). Similarly, the effective interaction strength, between a resonator j and a flux-tunable transmon i, reads

$$\bar{g}_{j,i}(t) = G_{j,i} \sqrt[4]{\frac{E_{J_i\text{eff}}(t)}{8E_{C_i}}}. \tag{20}$$

We find that the effective interaction strength is now time dependent. Note that this time dependence is often neglected, see Refs. [4, 7–9]. It is often the case, that the complete effective Hamiltonian is expressed solely in terms of bosonic operators $\hat{b}$ and $\hat{b}^\dagger$. In this representation the effective model Hamiltonian for architecture I reads

$$\begin{aligned}\hat{H}_I^{\text{eff}} &= \omega_2(t)\hat{b}_2^\dagger\hat{b}_2 + \frac{\alpha_2}{2}\hat{b}_2^\dagger\hat{b}_2(\hat{b}_2^\dagger\hat{b}_2 - \hat{I}) \\ &+ \omega_1\hat{b}_1^\dagger\hat{b}_1 + \frac{\alpha_1}{2}\hat{b}_1^\dagger\hat{b}_1(\hat{b}_1^\dagger\hat{b}_1 - \hat{I}) \\ &+ \omega_0\hat{b}_0^\dagger\hat{b}_0 + \frac{\alpha_0}{2}\hat{b}_0^\dagger\hat{b}_0(\hat{b}_0^\dagger\hat{b}_0 - \hat{I}) \\ &+ g_{2,1}(t)(\hat{b}_2^\dagger + \hat{b}_2)(\hat{b}_1^\dagger + \hat{b}_1) + g_{2,0}(t)(\hat{b}_2^\dagger + \hat{b}_2)(\hat{b}_0^\dagger + \hat{b}_0).\end{aligned} \tag{21}$$

TABLE III. Parameters for an effective Hamiltonian model of architecture I, see Table I and Eq. (7) for details and units.

i	$\omega/2\pi$	$\alpha/2\pi$	φ_0/π	$g_{2,i}(\varphi_0)$
0	5.100	-0.310	n/a	0.146
1	6.200	-0.285	n/a	0.164
2	8.100	-0.235	0.15	n/a

TABLE IV. Parameters for an effective Hamiltonian model of architecture II, see Table II and Eq. (8) for details and units.

i	$\omega^R/2\pi$	$\omega/2\pi$	$\alpha/2\pi$	$\varphi_0/2\pi$	$g_{2,i}(\varphi_0)$
0	n/a	4.200	-0.320	0	0.307
1	n/a	5.200	-0.295	0	0.344
2	45.000	n/a	n/a	n/a	n/a

Similarly, the effective model Hamiltonian for architecture II can be expressed as

$$\begin{aligned}\hat{H}_{II}^{\text{eff}} &= \omega_2^R \hat{a}_2^\dagger \hat{a}_2 \\ &+ \omega_1(t)\hat{b}_1^\dagger\hat{b}_1 + \frac{\alpha_1}{2}\hat{b}_1^\dagger\hat{b}_1(\hat{b}_1^\dagger\hat{b}_1 - \hat{I}) \\ &+ \omega_0(t)\hat{b}_0^\dagger\hat{b}_0 + \frac{\alpha_0}{2}\hat{b}_0^\dagger\hat{b}_0(\hat{b}_0^\dagger\hat{b}_0 - \hat{I}) \\ &+ \bar{g}_{2,1}(t)(\hat{a}_2^\dagger + \hat{a}_2)(\hat{b}_2^\dagger + \hat{b}_2) + \bar{g}_{2,0}(t)(\hat{a}_2^\dagger + \hat{a}_2)(\hat{b}_0^\dagger + \hat{b}_0).\end{aligned} \tag{22}$$

The device parameters that we use in our simulations to obtain the results in Sec. IV, are listed in Table III (for architecture I) and Table IV (for architecture II), respectively.

C. Control Pulse

All simulations in this work are performed with a control pulse (external flux) of the form

$$\varphi(t) = \varphi_0 + \delta e(t)\cos(\omega^D t), \tag{23}$$

where the real valued parameters φ_0, δ and ω^D denote the flux offset, the pulse amplitude and the drive frequency, respectively. The envelope function $e(t)$ is taken to be of the form

$$e(t) = \begin{cases} \sin(\lambda t) & \text{if } 0 \le t < T_{\text{r/f}} \\ 1 & \text{if } T_{\text{r/f}} \le t \le \Delta T \\ \sin(\frac{\pi}{2} + \lambda(t - \Delta T)) & \text{if } \Delta T < t \le T_{\text{d}}. \end{cases} \tag{24}$$

Here $T_{\text{r/f}}$ denotes the rise and fall time, T_{d} is the control pulse duration and $\Delta T = (T_{\text{d}} - T_{\text{r/f}})$. The parameter $\lambda = \pi/(2T_{\text{r/f}})$ is determined by the rise and fall time. This generic flux pulse allows us to control various transitions between states of the systems.

Figure 1 shows the external flux $\varphi/2\pi$ as a function of time for the two different types of flux control pulses we use in this work. Figure 1(a) shows a microwave pulse. Here we use Eq. (23), the amplitude $\delta/2\pi = 0.075$, the drive frequency $\omega^D/2\pi = 1.089$ GHz, a rise and fall time $T_{\text{r/f}} = 13$ ns and the pulse duration $T_{\text{d}} = 205.4$ ns. This type of control pulse is used for architecture I. Figure 1(b) shows a unimodal pulse. Here we use Eq. (23), the amplitude $\delta/2\pi = 0.297$, the drive frequency $\omega^D/2\pi = 0$ ns, a rise and fall time $T_{\text{r/f}} = 20$ ns and the pulse duration $T_{\text{d}} = 84$ ns. This type of control pulse is used to implement non-adiabatic gates [15] with architecture II.

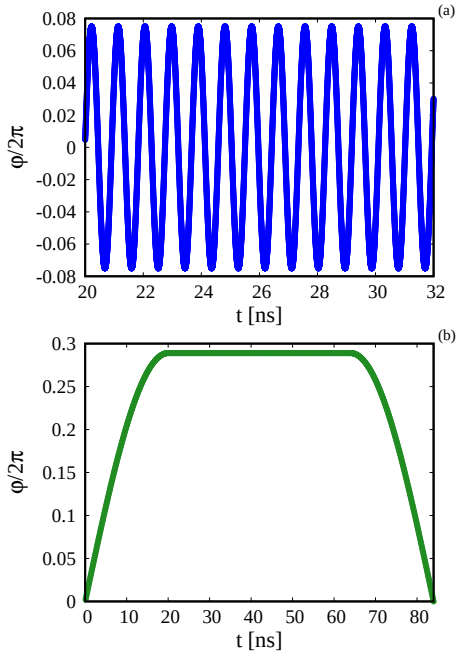

FIG. 1. (Color online) External flux $\varphi/2\pi$ as a function of time for two different flux control pulses. Figure 1(a): microwave pulse using Eq. (23), amplitude $\delta/2\pi = 0.075$, drive frequency $\omega^D/2\pi = 1.089$ GHz, a rise and fall time of $T_{\text{r/f}} = 13$ ns and pulse duration $T_{\text{d}} = 205.4$ ns. Figure 1(b): unimodal pulse using Eq. (23), amplitude $\delta/2\pi = 0.297$, drive frequency $\omega^D/2\pi = 0$ ns, a rise and fall time of $T_{\text{r/f}} = 20$ ns and pulse duration $T_{\text{d}} = 84$ ns.

III. SIMULATION ALGORITHM

In this section we discuss how we obtain the numerical results presented in Sec. IV.

The formal solution of the TDSE

$$i\partial_t |\Psi(t)\rangle = \hat{H}(t)|\Psi(t)\rangle, \tag{25}$$

with $\hbar = 1$ for an arbitrary time-dependent Hamiltonian $\hat{H}(t)$, reads

$$\hat{\mathcal{U}}(t, t_0) = \mathcal{T}\exp\left(-i\int_{t_0}^{t}\hat{H}(t')dt'\right), \tag{26}$$

where $\mathcal{T}$ is the time-ordering symbol. Numerical calculations require that this expression is discretised, with steps

of length τ. The corresponding time-evolution operator

$$\hat{U}(t+\tau,t) = \exp\left(-i\tau\hat{H}(t+\frac{\tau}{2})\right), \tag{27}$$

can then be implemented for every time step.

In this work we use the so-called product-formula algorithm [16, 17] to solve the TDSE. This algorithm is explicit, inherently unitary, and unconditionally stable by construction. Here the time step parameter τ needs to be chosen small enough, with respect to the energy scales and the other relevant time scales of $\hat{H}(t)$, such that the exact mathematical solution of the TDSE is obtained up to some fixed numerical precision. Practically, this means we decrease τ until it is small enough such that the relevant decimals do not change anymore. This procedure has to be repeated every time we make changes to the system, i.e. if we change the system parameters or the control pulse parameters.

Furthermore, for some computations, e.g. if we compute the spectrum of a Hamiltonian, we use a standard diagonalisation algorithm to obtain the eigenvalues and eigenstates of a Hamiltonian $\hat{H}(t)$.

For the simulations of the effective models, see Eqs. (21) and (22), we use four basis states for all transmons (fixed-frequency and/or flux-tunable) and also for the resonators. The simulation basis here consists of the bare, instantaneous basis states, see Sec. IV A for more details.

The simulations of the circuit Hamiltonian models are performed in the bare transmon basis, for more details see Appendix A. Here we use as many states as necessary, i.e. we increase the number of basis states N_m until the numerical values of the observables converge to some fixed numerical precision. This allows us to obtain an approximation free, numerical solution of the TDSE for the circuit Hamiltonian model.

IV. RESULTS

In this section we present our findings. First, in Sec. IV A, we consider a single isolated flux-tunable transmon. Here we focus on the transition dynamics and the spectrum of the system. Next, in Sec. IV B, we identify transitions (interactions) which seem to be suppressed in the effective model of architecture I, see Eq. (21). Finally, in Sec. IV C, we study how different approximations affect the unsuppressed transitions which are often used to implement two-qubit gates with architectures I and II.

A detailed discussion of all the results for all circuit Hamiltonians in Eqs. (2), (7) and (8) and the corresponding effective Hamiltonians in Eqs. (17), (21) and (22) exceeds the scope of a monograph. For this reason we provide a detailed discussion of the results for the circuit Hamiltonian simulations (where we do not make approximations to solve the TDSE) in Appendix A. A summary of the results for the circuit Hamiltonian simulations can be found in Table VI. Here we use the device parameters listed in Table I (architecture I) and Table II (architecture II) to obtain the results. In the following sections we compare these results with the ones we obtain by simulating the effective Hamiltonians Eqs. (17), (21) and (22) with the device parameters listed in Tables III and IV.

A. Simulations of a single flux-tunable transmon

The time evolution of the effective system described by $\hat{H}_{\rm tun}$, given in Eq. (17), is very simple. If we initialise the system in some arbitrary state

$$|\Psi^{\rm tun}(t_0)\rangle = \sum_{m=0,1,2,3} c_m(t_0)\,|m\rangle\,, \tag{28}$$

we obtain

$$|\Psi^{\rm tun}(t)\rangle = \sum_{m=0,1,2,3} e^{-i\int_{t_0}^{t} E^{(m)}(t')dt'} c_m(t_0)\,|m\rangle\,, \tag{29}$$

as the formal solution of the TDSE.

As one can see, the state population cannot change, no matter how we modulate the external flux $\varphi(t)$. If we consider the circuit Hamiltonian model, we find that there are several instances where this is not case. Note that we use the labels $\hat{H}_{\rm tun}$ and $\hat{H}_{\rm Tun}$ to differentiate between the effective (former) and the circuit (latter) model.

If we initialise the system in the lowest eigenstate $|\phi^{(0)}\rangle$ of Hamiltonian $\hat{H}_{\rm Tun}$, see Eq. (2) and apply a pulse of the form Eq. (23), see Fig. 1(a), with the parameters listed in Table VI, we find that the circuit Hamiltonian allows us to stimulate the transition $|\phi^{(0)}\rangle \to |\phi^{(1)}\rangle$. Note that in this scenario the drive frequency ω^D is set to the qubit frequency. These results for the circuit Hamiltonian model can be found in Appendix A, see Fig. 9. Clearly, the effective Hamiltonian $\hat{H}_{\rm tun}$ does not allow us to model such transitions.

The state vector Eq. (29) might also fail to reproduce the results of the circuit Hamiltonian model if we apply a fast changing unimodal flux pulse $\varphi(t)$, see Fig. 1(b). Figure 2 shows the quantity $1-p^{(m)}(T_{\rm d})$, for $m \in \{0,1,2,3\}$, as a function of the rise and fall time $T_{\rm r/f}$ and the pulse amplitude δ. Here

$$p^{(m)}(T_{\rm d}) = |\,\langle\phi^{(m)}|\Psi^{\rm Tun}(T_{\rm d})\rangle\,|^2, \tag{30}$$

denotes the probability of finding the system in the eigenstate $|\phi^{(m)}\rangle$ of circuit Hamiltonian Eq. (2) after the application of a pulse of the form Eq. (23) with $\omega^{\rm D} = 0$, $T_d = 50$ and $|\Psi^{\rm Tun}(0)\rangle = |\phi^{(m)}\rangle$. We use the circuit Hamiltonian Eq. (2) and the parameters listed in Table I ($i = 2$) to obtain the results. Figure 2 shows the cases for $m = 0$(a), $m = 1$(b), $m = 2$(c) and $m = 3$(d). As one can see, Fig. 2 shows that

$$1 - p^{(m)}(T_{\rm d}) \neq 0 \tag{31}$$

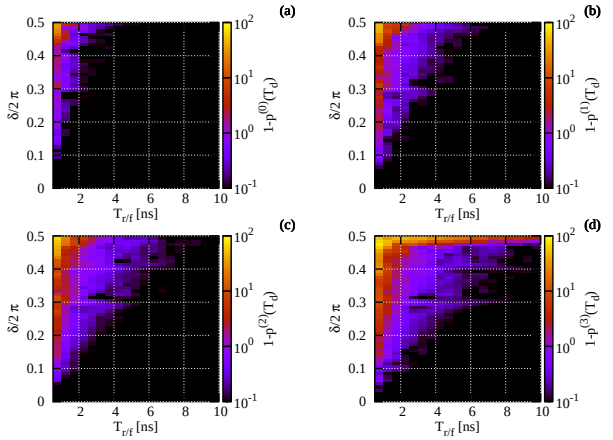

FIG. 2. (Color online) Probabilities $1-p^{(m)}(T_\mathrm{d})$ as functions of the rise and fall time $T_\mathrm{r/f}$ and the pulse amplitude δ for $m=0$(a), $m=1$(b), $m=2$(c) and $m=3$(d). The pulse duration is set to $T_\mathrm{d}=50$. We use circuit Hamiltonian Eq. (2), the pulse form Eq. (23) (with $\omega^D=0$) and the parameters listed in Table I ($i=2$) to obtain the results. The formal solution of the TDSE for the effective model and this specific scenario is given in Eq. (32). Since this solution is zero for all parameters and all $\varphi(t)$, we find that Fig. 2(a-d) show the deviations between the circuit and the effective model.

for various δ and $T_\mathrm{r/f}$. If we model the same scenario with the effective Hamiltonian Eq. (17), we find

$$1-|\langle\phi^{(m)}|\Psi^\mathrm{tun}(T_\mathrm{d})\rangle|^2=0, \tag{32}$$

for all m and all pulses $\varphi(t)$. The deviations are particularly large if $\delta\to 0.5$ and $T_\mathrm{r/f}\to 0$ (for all m). Furthermore, for the pulse we use here, it seems to be the case that higher states (see $m=2$ and $m=3$) suffer more from this effect. Certainly, this effect is not negligible when it comes to modelling fast two-qubit gates [18, 19]. It is likely that there exist better control pulses which minimise this effect. The functional form we use here was chosen such that we can drive all transitions with a single pulse form. However, it already shows that we can drive unexpected transitions of the system if we only consider the effective model for this pulse.

The formal solution in Eq. (29) is similar but not equivalent (in the sense that the solutions of the corresponding TDSEs only differ by a dynamic phase factor) to the non-degenerate adiabatic approximation [20]. Furthermore, it is well known that the adiabatic approximation fails to describe fast driven resonant transitions, for a detailed discussion of this issue see Ref. [21].

If we use Hamiltonian $\hat{H}_\mathrm{tun}$ to model the qubit, we make another assumption, namely that the spectrum can be approximated by the expression

$$\left(E^{(m)}(\varphi)-E^{(0)}(\varphi)\right)=\left(m\omega(\varphi)+\frac{\alpha(\varphi)}{2}m(m-1)\right). \tag{33}$$

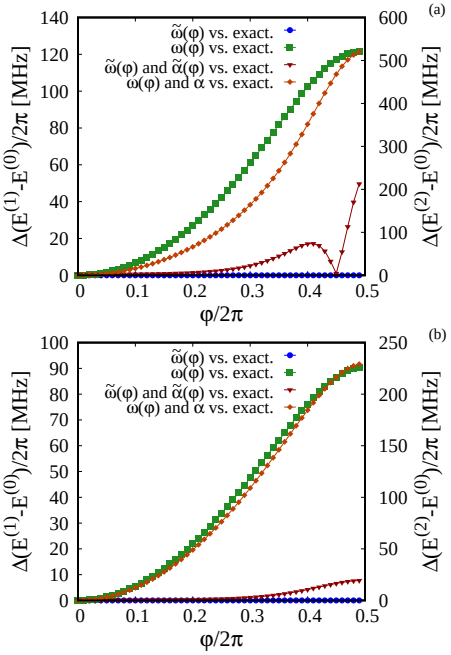

FIG. 3. (Color online) Deviations between the numerically exact spectrum and two different approximations of this spectrum as a function of the external flux φ for an asymmetry factor $d=0.33$(a) and $d=0.5$(b). First, we compute the numerically exact spectrum with 101 bare basis charge states. Then we use two different sets of expressions for the qubit frequency and anharmonicity to determine the approximated spectrum with Eq. (33). First case, $\omega(\varphi)$ is given by Eq. (16) and $\alpha(\varphi)=$ const.. Second case, $\tilde{\omega}(\varphi)$ is given by Eq. (B1) and $\tilde{\alpha}(\varphi)$ is given by Eq. (B2). In the end, we use Eq. (34) to determine the deviations between the numerically exact energies and the different approximants, cases one and two. We use the capacitive and Josephson energies as well as the qubit frequency and anharmonicity which are listed in Table I, row $i=2$. Note that for $m=1$ the deviations become independent of $\alpha(\varphi)$, see Eqs. (33) and (34). Therefore, we can label the different deviations by the functions we use for the qubit frequency and anharmonicity.

where $\omega(\varphi)$ is given by Eq. (16) and $\alpha(\varphi)$ is constant. Note that we temporarily removed the explicit time dependence $\varphi(t)\to\varphi$ since the spectrum exhibits symmetries with respect to the variable φ, see Hamiltonian Eq. (2).

Figure 3(a,b) shows the deviations

$$\Delta\left(E^{(m)}(\varphi)-E^{(0)}(\varphi)\right)=\Big|\left(E^{(m)}_\mathrm{exact.}(\varphi)-E^{(0)}_\mathrm{exact.}(\varphi)\right)-\left(m\omega(\varphi)+\frac{\alpha(\varphi)}{2}m(m-1)\right)\Big|, \tag{34}$$

for $m=1$ (on the left y-axis) and $m=2$ (on the right y-axis) between the numerically exact spectrum of Hamiltonian Eq. (2) and two different sets of expressions for the qubit frequency and anharmonicity in Eq. (34) as a

function of the external flux φ. First, we use the parameters listed in Table I, row $i = 2$, to compute the numerically exact values for two different asymmetry factors $d = 0.33$(a) and $d = 0.5$(b). Then we compute the approximated spectrum by means of Eq. (33). Here we consider two different cases. In the first case, we use Eq. (16) for $\omega(\varphi)$, $\alpha(\varphi) =$ const. and Eq. (33) to compute the energies. In the second case, we use the series expansions $\tilde{\omega}(\varphi)$, $\tilde{\alpha}(\varphi)$ (see Eqs. (B1) and (B2) respectively) and Eq. (33) to do the same. Both, Eqs. (B1) and (B2) were taken from Didier et al. [22]. Note that for $m = 1$, see Eqs. (33) and (34), the deviations between the different spectra become independent of $\alpha(\varphi)$. Therefore, we can label the different deviations by the functions we use to obtain the results.

As one can see, the first set of expressions Eq. (16) and $\alpha(t) =$ const. deviate more, from the exact solution, than Eqs. (B1) and (B2). In both cases, the deviations grow as the external flux φ approaches the value 0.5. Furthermore, the asymmetry factor d seems to influence how well the spectrum is approximated. If we compare Figs. 3(a,b), we find that in Fig. 3(b) the deviations can be smaller, e.g. by a factor of ten (compare right y-axis of Figs. 3(a,b)).

The deviations in the spectrum can change the behaviour of the system, once a flux pulse is applied. In particular, if we implement non-adiabatic two-qubit gates [15, 19], the spectrum determines whether or not transitions occur. This becomes even more important if we consider several flux-tunable transmon qubits in one system. Here the errors, in terms of the spectrum, might add up and enhance or suppress different transitions between states. Therefore, an accurate modelling of the spectrum is important.

In conclusion, the effective flux-tunable Hamiltonian does not allow us to model resonant transitions between the different states of the flux-tunable transmon. Also, non-adiabatic errors are suppressed, see Fig. 2. Furthermore, approximating the spectrum of the qubit by means of Eq. (16) and $\alpha =$ const. does not lead to very accurate results if we consider pulses $\varphi(t)$ with large amplitudes δ, see Eq. (23).

B. Simulations of suppressed transitions in the effective two-qubit model

In the previous section, we discussed the case of a single flux-tunable transmon. In this section we consider transitions in a two-qubit system which are suppressed in the effective model. Here we use the effective model Hamiltonian Eq. (21) and the parameters listed in Table III to obtain the results. The effective Hamiltonian describes a two-qubit system (two qubits and one coupler). We index the different states by using tuples of the form $z = (k_0, m_1, m_0)$, where $k_0 \in \{0, 1, 2, 3\}$ is the coupler index, $m_1 \in \{0, 1, 2, 3\}$ is the index of the second qubit and $m_0 \in \{0, 1, 2, 3\}$ is the index of the first qubit.

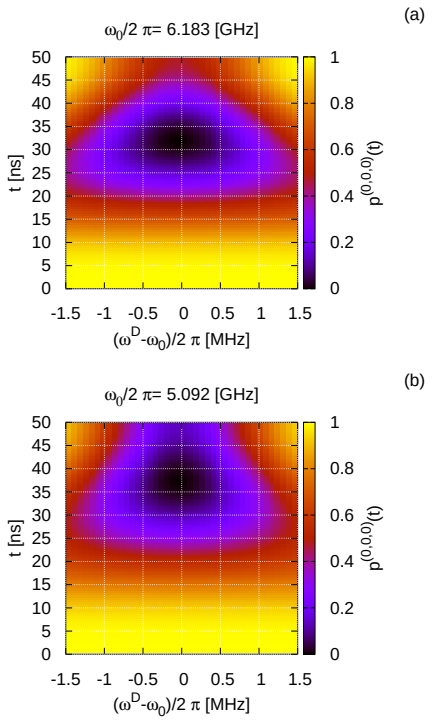

FIG. 4. (Color online) Chevron pattern (a), for a pulse of the form Eq. (23) with the drive frequency $\omega_0^{\mathrm{D}} = 6.183$ and the amplitude $\delta/2\pi = 0.005$. Chevron pattern (b), for a pulse of the form Eq. (23) with the drive frequency $\omega_0^{\mathrm{D}} = 5.092$ and the amplitude $\delta/2\pi = 0.009$. We use the same rise and fall time $T_{\mathrm{r/f}} = 13$ for both cases and a pulse duration T_{d} of around 50 ns. These patterns show how the circuit Hamiltonian Eq. (7) (with the parameters listed in Table I) reacts to two different pulses, characterised by the different pulse parameters. The color bar shows the probability $p^{(0,0,0)}(t)$ as a function of time t. The chevron patterns are used to calibrate control pulses, which are then used to obtain the results in Table VI.

Our aim is to model the following transitions $z = (0, 0, 0) \to z = (0, 1, 0)$ and $z = (0, 0, 0) \to z = (0, 0, 1)$ for a two-qubit system. We are able to model these transitions with the circuit Hamiltonian Eq. (7) and the device parameters listed in Table I, the pulse parameters are summarised in Table VI. However, we find that the effective model does not respond to pulses of the form Eq. (23), with pulse parameters similar to the ones given in Table VI. Therefore, we search for the corresponding transitions in a more systematic way.

We initialise the system in the state $z = (0, 0, 0)$ and compute the probability $p^{(0,0,0)}(\omega^D, \delta, t) = |\langle \phi^{(0,0,0)} | \Psi(\omega^{\mathrm{D}}, \delta, t) \rangle|^2$ for various control pulses, which are characterised by the drive frequency ω^{D} and the amplitude δ. This allows us to determine the function

$$\epsilon = 1 - \min_{(\omega^D, \delta, t) \in \mathcal{G}} (p^{(0,0,0)}(\omega^D, \delta, t)), \tag{35}$$

where $\mathcal{G} \subseteq \mathbb{R}^3$ denotes a grid which ranges over a discrete set of pulse parameters and a discrete set of points in time.

TABLE V. Results of the computation of the function $\epsilon = 1 - \min_{(\omega^{\mathrm{D}},\delta,t)\in\mathcal{G}}(p^{(0,0,0)}(\omega^{\mathrm{D}},\delta,t))$. Here ω^{D} denotes the drive frequency and δ is the pulse amplitude. The initial state of the system is $|\phi^{(0,0,0)}\rangle$ in all cases. The probability $p^{(0,0,0)}(\omega^D,\delta,t) = |\langle\phi^{(0,0,0)}|\Psi(\omega^D,\delta,t)\rangle|^2$ is determined for various pulses and points in times so that the minimum can be obtained. The first three columns show the search intervals for ω^D, δ and T_d, which define the search grid $(\omega^{\mathrm{D}},\delta,t) \in \mathcal{G} \subseteq \mathbb{R}^3$. The step parameters are set to $\Delta\omega/2\pi = 10^{-5}$ Ghz, $\Delta\delta/2\pi = 10^{-3}$ and $\Delta t = 0.2$ ns. The last column shows the result for ϵ. The results are obtained with the system parameters listed in Table III and effective Hamiltonian Eq. (21).

$\omega^D/2\pi$	$\delta/2\pi$	T_d	ϵ
$[4.90, 5.30]$	$[0.000, 0.110]$	$[0, 300]$	10^{-3}
$[6.00, 6.40]$	$[0.000, 0.110]$	$[0, 300]$	10^{-3}
$[0.00, 0.00]$	$[0.000, 0.000]$	$[0, 300]$	10^{-3}

Every row in Table V corresponds to a different search grid. In the first row we search for an excitation of the first qubit. This means we have to consider the frequency range $[4.90, 5.30]$. Similarly, in the second row we search in the frequency range $[6.00, 6.40]$. The last row serves as a reference. Here we simulate the free time evolution, i.e. we do not apply any external flux to the system. Since we do not want to activate transitions by accidentally creating an avoided crossing between different energies, we restrict the search range of the amplitude to $\delta/2\pi \in [0.000, 0.110]$. The step parameters are set to $\Delta\omega/2\pi = 10^{-5}$ GHz, $\Delta t = 0.2$ ns and $\Delta\delta/2\pi = 10^{-3}$. In all cases we find that $\epsilon \approx 0.001$. This means that the free time evolution yields the same result as the instances where we compute ϵ for various pulses. The results suggest that the system reacts to these sets of pulses in the same way it does to no pulse at all, i.e. the system remains mainly in its ground state.

Figure 4 shows two chevron patterns (obtained for the circuit Hamiltonian Eq. (7)). We used these figures to determine the pulse parameters for the results we presented in Table VI, see row three and four. The chevron patterns (a) and (b) are several MHz wide. Therefore, assuming that the effective Hamiltonian Eq. (21) allows us to model these operations, we would expect that $\epsilon \approx 1.000$. However, since this is not the case, we might conclude that we cannot model these transitions with Hamiltonian Eq. (21). Note that these results are in accordance with the single flux-tunable transmon case. Furthermore, there are other transitions, e.g. $z = (0, 0, 0) \to z = (1, 0, 0)$, which seem to be suppressed. Therefore, our listing is not complete. We leave this problem for future research.

The deficit of the effective model Hamiltonian that it does not describe all the transitions might become relevant once we consider more and more qubits in one system, i.e. if we consider the spectral crowding problem.

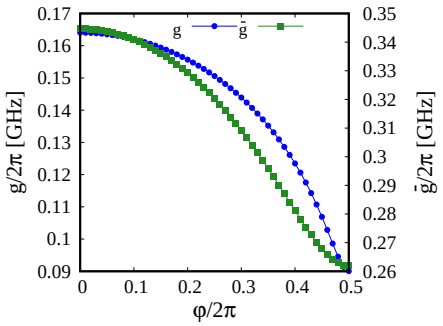

FIG. 5. (Color online) Effective interaction strengths g (see Eq. (19)) in blue on the left y-axis and $\bar{g}$ (see Eq. (20)) in green on the right y-axis as functions of the external flux φ. We use the energies listed in Table I ($i = 2$) to obtain g. Similarly, for $\bar{g}$ we use the parameters listed in Table II ($i = 1$).

C. Simulation of unsuppressed transitions in the effective two-qubit model

We studied, see Appendix A, transitions between states of the circuit Hamiltonian models which can be used to implement Iswap and Cz gates on different circuit architectures, see circuit Hamiltonians in Eqs. (7) and (8). In case of architecture I we applied a harmonic control pulse of the form Eq. (23) to the tunable coupler. On architecture II we activated transitions between different states by means of a unimodal pulse, i.e. in Eq. (23) we set $\omega^D = 0$. Here we create avoided crossings between different energy levels. More details are given in Appendix A. In this section we repeat this analysis with the effective model Hamiltonians in Eqs. (21) and (22) and compare the results with the ones for the circuit Hamiltonian models which can be found in Table VI. A summary of all results for the effective models can be found in Table VII.

It is common practice, see Refs. [4, 7–9], that multiqubit Hamiltonians are simplified by making assumptions about the effective parameters which influence the dynamics of the system. We begin this section with a discussion of one of these assumptions, namely that the effective interaction strength g (see Eqs. (21) and (22)) between the different subsystems is time independent.

Figure 5 shows the effective interaction strengths g (in blue on the left y-axis) for architecture I and $\bar{g}$ (in green on the right y-axis) for architecture II as functions of the external flux $\varphi/2\pi$. The values for $g(\varphi)$ were determined with Eq. (19) and the parameters listed in Table I ($i = 2$). Similarly, the values for $\bar{g}(\varphi)$ are obtained with the parameters listed in Table II ($i = 1$) and Eq. (20). We can see that both effective interaction strengths show a similar qualitative and quantitative behaviour. As one can see, $g(\varphi)$ varies around 0.075 GHz, over the interval $\varphi/2\pi \in [0, 0.5]$, while $\bar{g}(\varphi)$ spans over a range of 0.08 GHz.

Figure 6(a,b) shows the evolution of the effective interaction strength as a function of time. In Fig. 6(a)

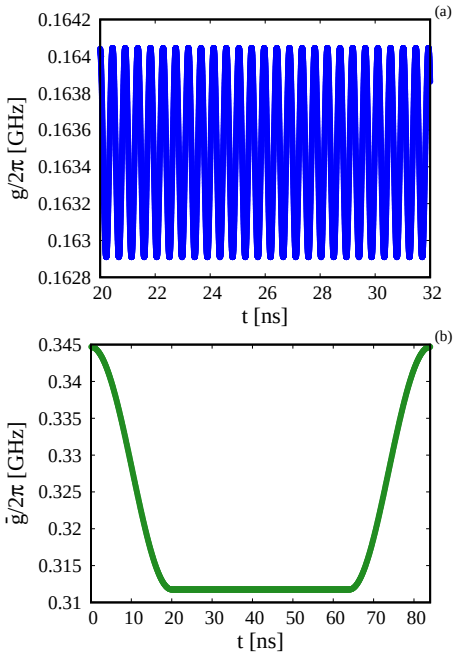

FIG. 6. (Color online) Effective interaction strength as a function of time for two different flux control pulses. Figure 6(a): effective interaction strength $g(\varphi(t))$ (see Eq. (19) and Eq. (23)) for architecture I. We use the energies listed in Table I ($i = 2$) to obtain g and the same control pulse parameters as in Fig. 1(a). These control pulse parameters are also listed in Table VII (row six). Figure 6(b): effective interaction strength $\bar{g}(\varphi(t))$ (see Eq. (20) and Eq. (23)) for architecture II. We use the energies listed Table II ($i = 1$) to obtain $\bar{g}$ and the same control pulse parameters as in Fig. 1(b). These control pulse parameters are also listed in Table VII (row nine).

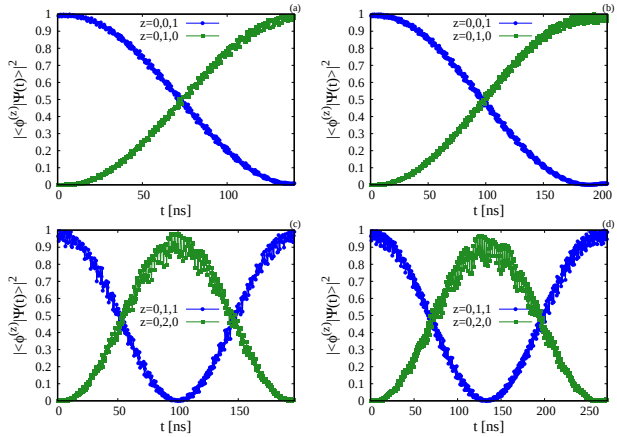

FIG. 7. (Color online) Panels (a) and (b): Probabilities $p^{(0,0,1)}(t)$ and $p^{(0,1,0)}(t)$ as functions of time t. Panels (c) and (d): Probabilities $p^{(0,1,1)}(t)$ and $p^{(0,2,0)}(t)$ as functions of time t. In panel (a,c) we model the system without a time-dependent effective interaction strength (see Eq. (19)). In panel (c,d) we include the time dependence. In all cases we use Hamiltonian Eq. (21), the parameters listed in Table III and a pulse of the form Eq. (23) to obtain the results. The pulse parameters are discussed in the main text. The $z = (0, 1, 1) \rightarrow z = (0, 2, 0)$ transitions are usually used to implement Cz operations and the $z = (0, 0, 1) \rightarrow z = (0, 1, 0)$ transitions are often used to realise Iswap operations, see Refs.[4, 12]. Interestingly, we observe a large shift in the pulse duration T_d if we model the system with a time-dependent effective interaction strength, see Fig. 6(a).

we show the effective interaction strength $g(\varphi(t))$ (see Eq. (19) and Eq. (23)) for architecture I. Here we use the same parameters as in Fig. 1(a) to model the control pulse $\varphi(t)$ and the energies listed in Table I ($i = 2$) to obtain g. In this case we observe fast oscillating variations of g at the order of 1 MHz. Similarly, in Fig. 6(b) we show the effective interaction strength $\bar{g}(\varphi(t))$ (see Eq. (20) and Eq. (23)) for architecture II. Here we use the same control pulse parameters as in Fig. 1(b) and the energies listed in Table II ($i = 1$). As one can see, in this case we find that if the pulse has reached its plateau, the effective interaction strength has been reduced by about 35 MHz.

Since architecture I is usually operated around a fixed flux offset φ_0, i.e. we only use small pulse amplitudes δ, we would expect that small variations of the effective interaction do not matter too much. The same reasoning would suggest that, in case of architecture II, the time-dependence of $\bar{g}(\varphi)$ is much more relevant since here we vary the external flux over a much larger interval. Furthermore, the unimodal pulse lowers the effective interaction strength temporarily, for about eighty percent of the total gate duration, and it does not oscillate. However, in the following section we show that this reasoning is not sound. We find that the time-dependent effective interaction strength affects architecture I much more than architecture II. We show this by performing all simulations twice, i.e. we simulate the systems with and without a time-dependent interaction strength.

1. *Architecture I*

We consider the model Hamiltonian Eq. (21). The simulation parameters are listed in Table III. We first discuss the two different Iswap transitions (see Figs. 7(a,b)) and then the Cz transitions (see Figs. 7(c,d)).

Figure 7(a) shows the probabilities $p^{(0,0,1)}(t)$ and $p^{(0,1,0)}(t)$ as functions of time t. We use a static effective interaction strength g to model the system, i.e. we use the effective interaction strength which is determined by the flux offset $\varphi_0/2\pi = 0.15$. We find a resonance frequency or optimal drive frequency of $\omega^D = 1.088$ GHz. This frequency deviates only 2 MHz from the one we found for the corresponding circuit Hamiltonian model, see Table VI. The drive amplitude which is $\delta/2\pi = 0.075$, is the same amplitude we use in Table VI. However, with these pulse parameters we find a gate duration of 139.6 ns. This means we can implement this gate around 70 ns faster than in the case of the circuit Hamiltonian Eq. (7), see Table VI. This is a rather strong difference.

TABLE VI. Summary of all model and pulse parameters used to perform simulations of the circuit Hamiltonians Eqs. (7) and (8), see Appendix A. The first column lists the model Hamiltonian and the system parameters (in form of references). The second column states which gate is modelled. The third column gives the states which are being controlled. The next columns show the following pulse parameters: the drive frequency $\omega^D/2\pi$ in GHz, the amplitude $\delta/2\pi$ in units of the flux quantum ϕ_0, the rise and fall time $T_{\mathrm{r/f}}$ in ns and the gate duration T_{d} in ns. The last column shows the number of basis states N_m which are needed to obtain an accurate solution.

Hamiltonian and parameters	Gate	States z	$\omega^D/2\pi$	$\delta/2\pi$	$T_{\mathrm{r/f}}$	T_{d}	N_m
Eq. (2) and Table I	X	$\{(0),(1)\}$	8.100	0.0001	10	20	3
Eq. (2) and Table I	X	$\{(0),(1)\}$	8.100	0.001	100	200	3
Eq. (7) and Table I	X	$\{(0,0,0),(0,1,0)\}$	6.183	0.005	22.5	45	3
Eq. (7) and Table I	X	$\{(0,0,0),(0,0,1)\}$	5.092	0.009	25	50	3
Eq. (7) and Table I	Iswap	$\{(0,1,0),(0,0,1)\}$	1.089	0.075	13	209.40	6
Eq. (7) and Table I	Cz	$\{(0,1,1),(0,2,0)\}$	0.809	0.085	13	297.55	8
Eq. (8) and Table II	Iswap	$\{(0,1,0),(0,0,1)\}$	0	0.289	20	100	14
Eq. (8) and Table II	Cz	$\{(0,1,1),(0,0,2)\}$	0	0.3335	20	125	16

TABLE VII. Summary of all pulse parameters we use to perform the simulations of the effective models Eq. (17), Eqs. (21) and (22). The first column lists the model Hamiltonian and the system parameters (in form of references). The second column shows which case we simulate. In case A we use a static interaction strength and a non-adjusted spectrum to model the system. In case B we use a time-dependent interaction and a non-adjusted spectrum to obtain the results. Similarly, in case C we use a time-dependent interaction strength and an adjusted spectrum. The third column displays the figure which contains the results. The fourth column states which gate we model. The fifth column shows the states which are being controlled. The next columns show the following pulse parameters: the drive frequency $\omega^D/2\pi$ in GHz, the amplitude $\delta/2\pi$ in units of the flux quantum ϕ_0, the rise and fall time $T_{\mathrm{r/f}}$ in ns and the gate duration T_{d} in ns. In the last column we state whether or not is was possible to model the gate (see Sec. IV B for more details). If it is not possible to model a transition, we label the corresponding parameters with not applicable (n/a).

Hamiltonian and parameters	Case	Fig.	Gate	States z	$\omega^D/2\pi$	$\delta/2\pi$	$T_{\mathrm{r/f}}$	T_{d}	Can be modeled?
Eq. (17) and Table III	n/a	n/a	X	$\{(0),(1)\}$	n/a	n/a	n/a	n/a	No
Eq. (17) and Table III	n/a	n/a	X	$\{(0),(1)\}$	n/a	n/a	n/a	n/a	No
Eq. (21) and Table III	n/a	n/a	X	$\{(0,0,0),(0,1,0)\}$	n/a	n/a	n/a	n/a	No
Eq. (21) and Table III	n/a	n/a	X	$\{(0,0,0),(0,0,1)\}$	n/a	n/a	n/a	n/a	No
Eq. (21) and Table III	A	Fig. 7(a)	Iswap	$\{(0,1,0),(0,0,1)\}$	1.088	0.075	13	139.6	Yes
Eq. (21) and Table III	B	Fig. 7(b)	Iswap	$\{(0,1,0),(0,0,1)\}$	1.089	0.075	13	205.4	Yes
Eq. (21) and Table III	A	Fig. 7(c)	Cz	$\{(0,1,1),(0,2,0)\}$	0.807	0.085	13	196.5	Yes
Eq. (21) and Table III	B	Fig. 7(d)	Cz	$\{(0,1,1),(0,2,0)\}$	0.807	0.085	13	272.00	Yes
Eq. (22) and Table IV	A	Fig. 8(a)	Iswap	$\{(0,1,0),(0,0,1)\}$	0	0.297	20	84	Yes
Eq. (22) and Table IV	C	Fig. 8(b)	Iswap	$\{(0,1,0),(0,0,1)\}$	0	0.289	20	96	Yes
Eq. (22) and Table IV	A	Fig. 8(c)	Cz	$\{(0,1,1),(0,0,2)\}$	0	0.343	20	105	Yes
Eq. (22) and Table IV	C	Fig. 8(d)	Cz	$\{(0,1,1),(0,0,2)\}$	0	0.334	20	121	Yes

Figure 7(b) shows the probabilities $p^{(0,0,1)}(t)$ and $p^{(0,1,0)}(t)$ as functions of time t. We use a time-dependent effective interaction strength to model the dynamics of the system.

Note that the effective interaction strengths $g(\varphi)$ for an external flux of $\varphi/2\pi = 0.075$ and $\varphi/2\pi = 0.15$ deviate from one another by roughly 3 MHz. Furthermore, the $\bar{g}(\varphi)$'s for an external flux of $\varphi/2\pi = 0.225$ and $\varphi/2\pi = 0.15$ deviate from one another by roughly 10 MHz. Apart from the effective interaction strength, we only adjusted the drive frequency slightly. Here we find an optimal drive frequency of $\omega^D = 1.089$ GHz. As one can see, the gate duration in this case is 205.4 ns. Therefore, we find that the deviations between the gate durations, for both models Eqs. (7) and (21), decrease to 4 ns if we model the system with a time-dependent interaction strength.

Figures 7(c,d) show the same scenarios for the Cz operation, i.e. we display the time evolution of $p^{(0,1,1)}(t)$ and $p^{(0,2,0)}(t)$ for two different models. In Fig. 7(c) we model the system with a time-independent effective interaction strength and in Fig. 7(d) we include the time dependence. In both cases we find the optimal drive frequency $\omega^D = 0.807$ GHz. If we compare this drive frequency with the one we obtained for the circuit Hamiltonian, see Table VI, we see that there is a shift of 2 MHz. Additionally, both control pulses are calibrated with an

amplitude of $\delta/2\pi = 0.085$.

We observe that if we model the system with a time-independent effective interaction strength, we find a gate duration of 196.5 ns. Including the time dependence leads to a gate duration of 272 ns. A comparison between theses results and the ones given in Appendix A leads to a deviation of around 25 ns if we include the time-dependent effective interaction strength.

This leads to the question why the oscillations of the effective interaction strength $g(t)$ are so relevant. It is possible that the time-dependent effective interaction strength induces a time-dependent shift of the resonance frequency. Consequently, we would consider a system that is only partially in a resonant state, i.e. the resonance frequency oscillates around the drive frequency.

The remaining differences might be attributed to additional approximations which have been made. For instance, we model the interaction between the different subsystems with an operator which is the result of a perturbative analysis, see Koch et al. [10]. D. Willsch [23] showed that such approximations can lead to deviations which increase with time; in this case a free time evolution was considered.

In general, we find that if we consider short timescales of around 250 ns, both Hamiltonians in Eq. (7) and Eq. (22), predict similar outcomes for only marginally different control pulses if we model the system with a time-dependent interaction strength.

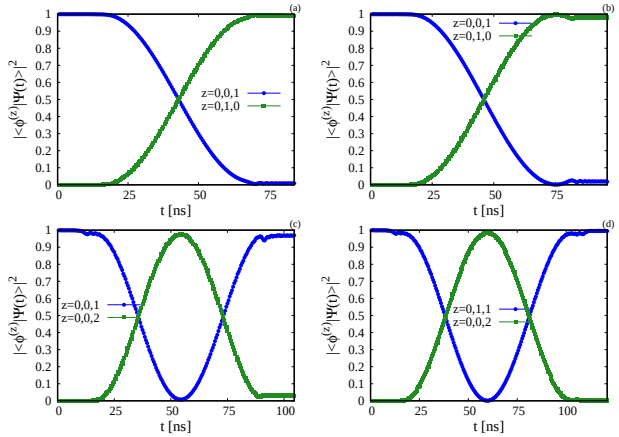

FIG. 8. (Color online) Panels (a) and (b): Probabilities $p^{(0,0,1)}(t)$ and $p^{(0,1,0)}(t)$ as functions of time t. Panels (c) and (d): Probabilities $p^{(0,1,1)}(t)$ and $p^{(0,0,2)}(t)$ as functions of time t. In panel (a,c) we model the system without a time-dependent effective interaction strength (see Eq. (20)). In panel (c,d) we include the time dependence. In all cases we use Hamiltonian Eq. (22), the parameters listed in Table IV and a pulse of the form Eq. (23) to obtain the results. The pulse parameters are discussed in the main text. The $z = (0,1,1) \rightarrow z = (0,2,0)$ transitions are usually used to implement Cz operations and the $z = (0,0,1) \rightarrow z = (0,1,0)$ transitions are often used to realise Iswap operations. We observe a modest shift in the pulse duration T_d if we model the system with a time-dependent effective interaction strength, see Fig. 6(b).

2. *Architecture II*

In the following, we compare the results of the second circuit Hamiltonian Eq. (8) with the ones we obtain for Hamiltonian Eq. (22). Here we use the parameters listed in Table IV to obtain the results. Furthermore, we use a pulse of the form Eq. (23) with $\omega^\mathrm{D} = 0$ and $T_{\mathrm{r/f}} = 20$ ns in all cases. As before, we first discuss the Iswap gate (see Figs. 8(a,b)) and then the Cz gate (see Figs. 8(c,d)).

Figure 8(a) shows the probabilities $p^{(0,0,1)}(t)$ and $p^{(0,1,0)}(t)$ as functions of time t. We use a time-independent effective interaction strength to model the dynamics of the system. We find the optimal drive amplitude $\delta/2\pi = 0.297$ and a gate duration of $T_\mathrm{d} = 84$ ns. Consequently, we observe a 16 ns discrepancy if we compare these results with the one we obtained for the circuit Hamiltonian model, see Table VI. Furthermore, the pulse amplitude has shifted. This can be explained by the fact that the flux-tunable frequency of the effective model $\omega(\varphi)$ as well as the corresponding anharmonicity α start to deviate from the numerically exact spectrum for large external fluxes φ, see Eq. (34) and Fig. 3.

We can correct the spectrum by using more accurate expressions (see Eqs. (B1) and (B2)) for the qubit frequency and the anharmonicity. Figure 8(b) shows the probabilities $p^{(0,0,1)}(t)$ and $p^{(0,1,0)}(t)$ as functions of time t. Here we model the system with a time-dependent effective interaction strength $\bar{g}(t)$ (see Eq. (20)). Furthermore, we also adjust the spectrum. We find the optimal pulse amplitude $\delta/2\pi = 0.289$. This is the same amplitude we determined for the circuit Hamiltonian Eq. (8), see Table VI. We find a gate duration of 96 ns. Therefore, the discrepancies between the different gate duration times have decreased to 4 ns. Note that this is the same deviation we found for the other system, when we modelled the Iswap operation.

We also simulated the case (data not shown) where only the spectrum is adjusted and the effective interaction strength is constant. As before, we compute the tunable qubit frequency and anharmonicity with the series expansions in Eqs. (B1) and (B2). Here we also find an optimal pulse amplitude $\delta/2\pi = 0.289$. Therefore, we conclude that this is purely a consequence of the deviations in the qubit frequency and anharmonicity, see Fig. 3.

Figure 8(c,d) show the probabilities $p^{(0,1,1)}(t)$ and $p^{(0,0,2)}(t)$ as functions of time t. Here we model the Cz gate with two different model Hamiltonians, i.e. with and without the time-independent effective interaction strength and an adjusted spectrum. Figure 8(c,d) show the same characteristics as Figs. 8(a,b). We find that if we do not use an adjusted spectrum, the optimal control pulse amplitude δ experiences a shift. Furthermore, if we assume that the effective interaction strength is constant, we find a gate duration which is about 20 ns shorter. If

we adjust the spectrum, we find that the shift of the optimal drive amplitude disappears. Similarly, if we include the time-dependent effective interaction strength, we see that the gate duration increases to 121 ns. This means the differences between the effective and the circuit Hamiltonian model decrease to 4 ns. Therefore we might conclude that the time-dependence of the effective interaction strength is not negligible if the aim is to approximate the time evolution of the corresponding circuit Hamiltonian.

In summary, we observe that if we adjust the spectrum of the effective Hamiltonian and include the time dependence of the effective interaction strength, the effective and the circuit Hamiltonian models predict similar outcomes. However, we also find that if the model is not adjusted properly, the outcomes can deviate quite strongly. Note that the deviations are already observable for the rather small time scales considered here, and such deviations typically tend to grow with time.

V. SUMMARY AND CONCLUSIONS

For this work we have implemented two simulation codes to solve the TDSE for two different but related generic models of a superconducting quantum processor. The first model is a lumped-element model, i.e here we consider a circuit Hamiltonian. The second model is an approximation of the first one, i.e. here we consider an effective model Hamiltonian. Both models aim to describe a set of interacting transmon qubits (fixed-frequency and/or flux-tunable) and transmission line resonators. The interaction between the different subsystems is always of the dipole-dipole type.

The first simulation code, for the circuit Hamiltonian model, enables us to simulate the model without making any approximations. The second simulation code, for the effective Hamiltonian model, allows us to simulate the system with various approximations being turned on or off. A basic version of the simulation code for the effective model is available on JuGit, see Ref. [24]. This simulation framework provides us with the tools to study the validity of different approximations, which are often made to make analytical calculations feasible.

For our study we consider three different systems. The first system is a single flux-tunable transmon. The second system (architecture I) consists of two fixed-frequency transmons, coupled to a flux-tunable transmon (this transmon works as a coupler). The third system (architecture II) is made up of two flux-tunable transmons, coupled to a transmission line resonator (this resonator functions only as a coupler element).

We have found that the spectrum, determined by the most commonly used approximation Eq. (16), of the single flux-tunable transmon system can deviate quite strongly (several hundred MHz, depending on which energy level is considered) from the numerically exact spectrum of the corresponding circuit Hamiltonian. Such deviations can become very important if we construct larger systems, where the energy levels are much more narrowly spaced. If possible, we suggest to use the series expansions Eqs. (B1) and (B2), which were given by Didier et al. [22], to remedy this issue. The corresponding deviations are much smaller, at least for the parameters we have tested.

We also found that approximating the flux-tunable transmon Hamiltonian Eq. (2) by the effective model Hamiltonian Eq. (17), prevents us from describing resonant transitions between the eigenstates of the isolated flux-tunable transmon Hamiltonian. In addition, it seems that this approximation also affects resonant transitions which are present in multi-qubit systems, e.g. architecture I. A summary of these results is provided in Table VII, see rightmost column. Note that this table is not complete, there are more resonant transitions which cannot be modelled with the effective Hamiltonian Eq. (21). Once we build larger superconducting processors, with more than a few transmon qubits, we have to acknowledge the problem of spectral crowding. However, if we base our analysis of this problem only on the transition frequencies which are relevant for the effective model, we might overlook frequencies which are crucial for this issue. Furthermore, it should be obvious that all non-adiabatic errors, see Fig. 2 in Sec. IV A, cannot be modelled with the effective model. This issue might be particularly relevant for architecture I, which uses a fast oscillating flux pulse. If possible, one should avoid too large amplitudes and drive frequencies, in order to minimise leakage into other states.

It also turned out, see Sec. IV C, that assuming that the effective interaction strength is time independent affects the gate durations quite strongly. A summary of these results can be found in Table VII, see the second-last column. Here we consider the difference between two effective models (with and without a time-dependent interaction strength) and the difference with respect to the circuit Hamiltonian model. The largest deviations can be found for architecture I, here one can find cases where the gate duration deviates up to about 100 ns. These deviations seem too large to be neglected. We also provide a reasonable explanation for these strong deviations. It might be that the time-dependent interaction strength induces a time-dependent shift of the resonance frequency. Consequently, the system would only partially (for some moments in time) be in a resonant state.

So far we limited our analysis to the dynamics of the very basic state transition mechanism. For future work, it might be interesting to see whether or not the different models generate different error signatures, when complete quantum circuits are simulated (see Willsch et al. [25]). It is likely that these errors are very sensitive to changes in the model. The challenge here is to make a fair comparison between two different models that are parameterised in terms of the pulse parameters.

VI. ACKNOWLEDGMENTS

The authors gratefully acknowledge the Gauss Centre for Supercomputing e.V. (www.gauss-centre.eu) for funding this project by providing computing time on the GCS Supercomputer JUWELS [26] at Jülich Supercomputing Centre (JSC). H.L. acknowledges support from the project OpenSuperQ (820363) of the EU Quantum Flagship.

Appendix A: Circuit Hamiltonian simulations

In this appendix we discuss the results of the circuit Hamiltonian simulations. A summary of the relevant results, for the main part of this work, can be found in Table VI. We begin with a discussion of the simulation details in Sec. A 1. Then, in Sec. A 2, we discuss the transitions which are suppressed in the effective model, see Sec. IV B. In the end, in Sec. A 3, we discuss the transitions which are unsuppressed in the effective model, see Sec. IV C.

1. Simulation of circuit Hamiltonians in the transmon basis

If we intend to simulate the circuit Hamiltonians given in Eq. (2), Eqs. (7) and (8) without performing any approximations, we can perform the simulations in the transmon bare basis

$$|\phi^{(z)}\rangle = \bigotimes_{j=0}^{J-1} |\phi^{(m_j)}\rangle\,, \tag{A1}$$

where $z = m_0, ..., m_{J-1}$ is a placeholder for the different subsystem indices m_j. We form this basis by means of the bare basis states

$$|\phi^{(m_j)}\rangle\,, \tag{A2}$$

of the corresponding subsystems. These states are the eigenstates of the Hamiltonians given in Eq. (1), Eq. (2) and Eq. (4) at time $t = 0$. For simplicity, we call this basis the transmon basis. We need to be able to change the number of basis states N_m, to allow us to extend the basis up to the point where the relevant decimals of our observables do not change anymore. The numerical error which stems from the discretisation of the time domain can be controlled by decreasing the time grid parameter τ, see Eq. (27), up to a point where convergence has been reached. Obviously, both parameters N_m and τ have to be changed together

In this work, we are satisfied if the probabilities

$$p^{(z)}(t) = |\,\langle\phi^{(z)}|\Psi(t)\rangle\,|^2, \tag{A3}$$

we are interested in converge to the third decimal. Here $|\Psi(t)\rangle$ denotes the solution of the TDSE. Note that we use at least three basis states for the transmons in the system. If not stated otherwise, transmission line resonators are modelled with four states.

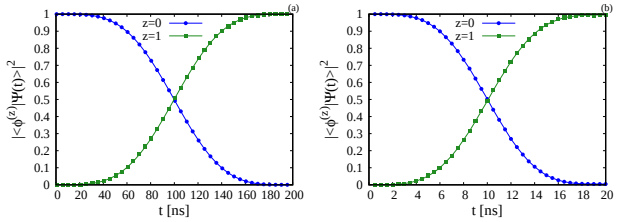

FIG. 9. (Color online) Probabilities $p^{(0)}(t)$ and $p^{(1)}(t)$ as functions of time t. We use three transmon basis states $N_m = 3$ to model the dynamics of the system, a control pulse of the form Eq. (23) and a drive frequency ω^D equal to the qubit frequency ω (see Table I, row $i = 2$). The rise and fall time $T_{\mathrm{r/f}}$ is set to half the duration time T_{d}. The system is initialised in the state $|\psi^{(0)}\rangle$. The pulse amplitude $\delta/2\pi$ is set to (a) $\delta/2\pi = 0.001$ and (b) $\delta/2\pi = 0.0001$. We can observe that an increase in the pulse amplitude δ by a factor of ten, leads to a decrease of the pulse duration T_{d} by a factor of ten (rougly). Note that these transitions cannot be modelled with the effective Hamiltonian Eq. (17).

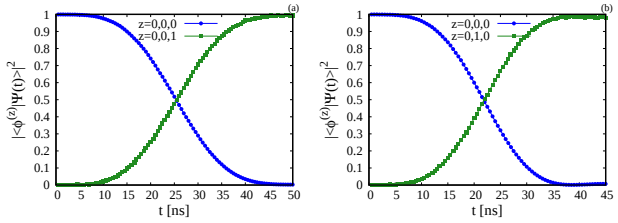

FIG. 10. (Color online) Probabilities $p^{(z)}(t)$ for (a) $z = (0, 0, 0)$ and $z = (0, 0, 1)$ and (b) $z = (0, 0, 0)$ and $z = (0, 1, 0)$ as a function of time t. In both cases we use three basis states $N_m = 3$ to model the dynamics of the system, a control pulse of the form Eq. (23) and a rise and fall time $T_{\mathrm{r/f}}$ set to half the duration time T_{d}. (a) We use the drive frequency $\omega^D = 5.092$ GHz, the pulse amplitude $\delta/2\pi = 0.009$. (b) We use the drive frequency $\omega^D = 6.183$ GHz and the pulse amplitude $\delta/2\pi = 0.005$. The initial state of the system is always $|\psi^{(0,0,0)}\rangle$. Note that we were not able to activate these transitions in the effective model of architecture I, see Hamiltonian Eq. (21).

2. Circuit Hamiltonian simulations of transitions that are suppressed in the effective model

We start our discussion with a single, isolated flux-tunable transmon. The system itself is defined by the parameters in Table I and we model the system with circuit Hamiltonian Eq. (2). Here we consider the flux-tunable transmon with label $i = 2$. Figure 9(a) shows the time evolution of the probabilities $p^{(z)}(t)$, for the two lowest eigenstates $z \in \{0, 1\}$. We use a control pulse of the form Eq. (23), see Fig. 1(a), where we set ω^{D} equal to the qubit frequency ω. The rise and fall time $T_{\mathrm{r/f}}$ is set to half of the pulse duration T_{d}. The x-axis displays

the duration time. The pulse amplitude in this case is set to $\delta/2\pi = 0.0001$.

As one can see, the system is initially in the state $|\phi^{(0)}\rangle$ and we are able to implement a smooth transition between the states $|\phi^{(0)}\rangle$ and $|\phi^{(1)}\rangle$.

Figure 9(b) shows the results for a similar scenario. Here we increased the amplitude by one order of magnitude, i.e. we use $\delta/2\pi = 0.001$. The time evolution shows that the duration $T_{\rm d}$ has decreased roughly by a factor of ten. Note that the transitions between the states $|\phi^0\rangle$ and $|\phi^1\rangle$ cannot be modelled with the effective Hamiltonian Eq. (17).

In both cases it is sufficient to use three basis states to model the dynamics of the system, i.e. increasing the number of basis states above three has no real impact on the probabilities we are interested in.

While it is possible to generate similar results (data not shown) for amplitudes in the range $\delta/2\pi \in [0.0001, 0.001]$ we find that for amplitudes $\delta/2\pi \gg 0.001$ it is not possible to implement a smooth transition between both states. Here the pulse does not conserve the probability in the subspace $\{|\phi^{(0)}\rangle, |\phi^{(1)}\rangle\}$.

Next we study a system which consists of three transmons. We add two fixed-frequency transmons to the flux-tunable transmon. This means the corresponding circuit Hamiltonian is of the form Eq. (7). Table I shows the corresponding system parameters. These parameters are motivated by a series of experiments performed by Ganzhorn et al. [4]. Figures 10(a,b) show the system's response to a harmonic pulse of the form Eq. (23), see Fig. 1(a).

In Fig. 10(a) we use the drive frequency $\omega^D = 6.183$ and the amplitude $\delta/2\pi = 0.005$. Here the figure shows the probabilities $p^{(z)}(t)$, for $z = (0,0,0)$ and $z = (0,1,0)$, as a function of time t. In this case the intention is to drive the $z = (0,0,0) \rightarrow z = (0,1,0)$ transition.

Figure 10(b) shows a similar case. Here we use the drive frequency $\omega^D = 5.092$ and the amplitude $\delta/2\pi = 0.009$. Since we intend to drive the $z = (0,0,0) \rightarrow z = (0,0,1)$ transition, we display the corresponding probabilities $p^{(z)}(t)$ as a function of time t.

In both cases the initial state is set to $|\phi^{(0,0,0)}\rangle$ and we find a duration time $T_{\rm d}$ of around 50 ns.

Figures 10(a,b) show that we are able to implement transitions between the state pairs $z = (0,0,0)$ and $z = (0,1,0)$ as well as $z = (0,0,0)$ and $z = (0,0,1)$. In addition, it is also possible (data not shown) to drive transitions of the form $z = (0,0,1) \rightarrow z = (0,1,1)$ and $z = (0,1,0) \rightarrow z = (0,1,1)$, simply by changing the initial state of the system and leaving all other parameters. Note that we were not able to activate these transitions in the effective model of architecture I, see Hamiltonian Eq. (21). Here we do not consider the transmon $i = 2$ (see Table I) since it is considered to be a coupler and not an actual qubit. However, it is possible to drive the transition $z = (0,0,0) \rightarrow z = (1,0,0)$.

For both cases we find that it is sufficient to use three transmon basis states to model the dynamics of the system.

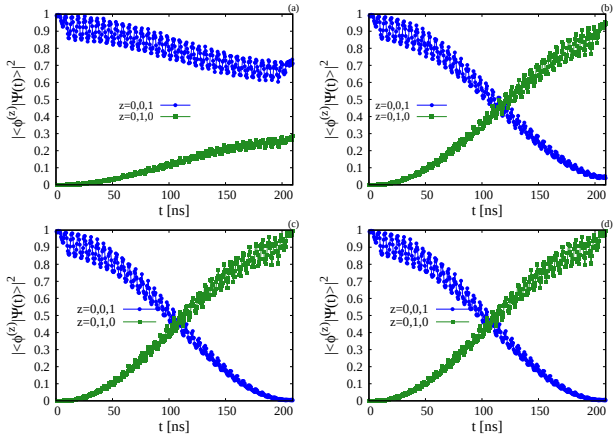

FIG. 11. (Color online) Probabilities $p^{(0,0,1)}(t)$ and $p^{(0,1,0)}(t)$ as functions of time t. We use $N_m = 3$ (a), $N_m = 4$ (b), $N_m = 6$ (c) and $N_m = 15$ (d) basis states to model the system. We use a control pulse of the form Eq. (23), with the pulse parameters $\omega^D = 1.089$ GHz, $T_{\rm r/f} = 13$ ns and $\delta/2\pi = 0.075$. The pulse duration is $T_{\rm d} = 209.40$ ns. The system we simulate is defined by Eq. (7) and Table I. The $z = (0,0,1) \rightarrow z = (0,1,0)$ transition is usually used to implement Iswap operations, see Refs. [4]. We find that numerical accurate modelling of the dynamic behaviour of the system seems to require at least $N_m = 6$ transmon basis states.

3. Circuit Hamiltonian simulations of the unsuppressed transitions in the effective two-qubit models

We investigate the transitions which are unsuppressed in the effective model. Here we differentiate between two cases. We first discuss transitions which are used to implement two-qubit gates by means of harmonic microwave pulses [4, 8, 9]. In this case we simulate circuit Hamiltonian Eq. (7), with the parameters listed in Table I. As a second case, we study transitions which are activated by unimodal pulses, i.e. gates which are implemented by means of adiabatic passage techniques [15, 27]. In this case we simulate circuit Hamiltonian Eq. (8). The corresponding system parameters can be found in Table II.

a. Architecture I

Figures 11(a-d) show the time evolution of the probabilities $p^{(0,0,1)}(t)$ and $p^{(0,1,0)}(t)$ as a function of time t. We use $N_m = 3$ (a), $N_m = 4$ (b), $N_m = 6$ (c) and $N_m = 15$ (d) basis states to model the dynamics of the system. The transition we model here is usually used to implement an Iswap gate. The drive frequency is $\omega^{\rm D} = 1.089$ GHz, which corresponds roughly to the frequency difference $\Delta\omega = 1.100$ GHz between the indi-

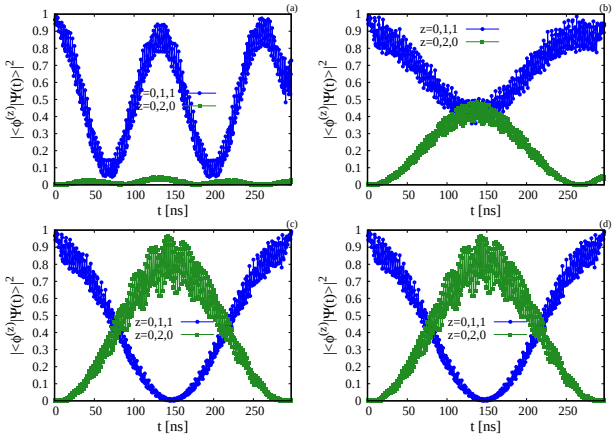

FIG. 12. (Color online) Probabilities $p^{(0,1,1)}(t)$ and $p^{(0,2,0)}(t)$ as functions of time t. We use $N_m = 3$ (a), $N_m = 4$ (b), $N_m = 8$ (c) and $N_m = 15$ (d) basis states to model the system. We use a control pulse of the form Eq. (23), with the pulse parameters $\omega^{\mathrm{D}} = 0.809$ GHz, $T_{\mathrm{r/f}} = 13$ ns and $\delta/2\pi = 0.085$. The pulse duration is $T_{\mathrm{d}} = 297.55$ ns. The system we simulate is defined by Eq. (7) and Table I. The $z = (0,1,1) \rightarrow z = (0,2,0)$ transition is usually used to implement Cz operations, see Refs. [4, 12]. We find that numerical accurate modelling of the dynamic behaviour of the system seems to require at least $N_m = 8$ transmon basis states.

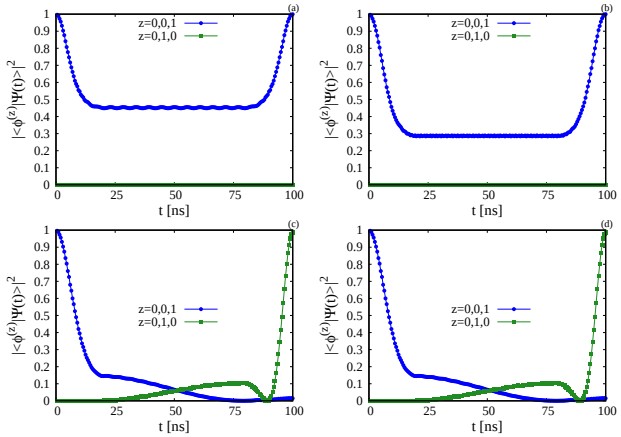

FIG. 13. (Color online) Probabilities $p^{(0,0,1)}(t)$ and $p^{(0,1,0)}(t)$ as functions of time t. We use $N_m = 3$ (a), $N_m = 4$ (b), $N_m = 14$ (c) and $N_m = 25$ (d) basis states to model the system. We use a control pulse of the form Eq. (23), with the pulse parameters $\omega^{D} = 0$ GHz, $T_{\mathrm{r/f}} = 20$ ns and $\delta/2\pi = 0.289$. The pulse duration is $T_{\mathrm{d}} = 100.00$ ns. The pulse is supposed to perform an Iswap gate. The system we simulate is defined by Eq. (8) and Table II. The $z = (0,0,1) \rightarrow z = (0,1,0)$ transition might be used to implement Iswap operations. Note that solutions in panel (a) and (b) do not have much in common with the reference solutions in panels (c) and (d).

vidual transmon qubits $i = 1$ and $i = 0$. The frequency shift stems from the fact that the states $\{|\phi^{(z)}\rangle\}$ are not exact eigenstates of the full circuit Hamiltonian. The drive amplitude is set to $\delta/2\pi = 0.075$ and the initial state of the system is $|\phi^{(0,0,1)}\rangle$.

The time evolutions in Figs. 11(a-d) clearly show that three or four basis states are not sufficient to describe this operation, i.e. if we compare the solutions (a) and (b) with the reference solution (c)/(d) we find substantial qualitative and quantitative differences. We find that we need at least six transmon basis states to model the system. Note that we simulated the same system before when studying the single-qubit operations. We conclude that the number of states which is needed to model different types can vary, i.e., it is not a system property but it depends on the type of transition we simulate.

Figures 12(a-d) show the time evolution of the probabilities $p^{(0,1,1)}(t)$ and $p^{(0,2,0)}(t)$ as a function of time t. We use $N_m = 3$ (a), $N_m = 4$ (b), $N_m = 8$ (c) and $N_m = 15$ (d) transmon basis states to model the system. This transition is often used to implement a Cz operation, see Ref. [12]. The corresponding drive frequency is $\omega^{\mathrm{D}} = 0.809$ GHz, which corresponds roughly to the energy difference, in GHz, of the two states involved. The pulse amplitude is $\delta/2\pi = 0.085$.

We observe that if we model this particular Cz operation, we find severe qualitative and quantitative deviations between the solutions (a) and (b) and (c)/(d) . Here we should use eight basis states to accurately model the dynamics of the system.

The Iswap and Cz operations we studied here are implemented with gate durations T_{d} between 200 and 300 ns. It is possible to implement shorter gate durations, by increasing the amplitude (data not shown). However, this almost always means we have to increase the number of basis states N_m to obtain an accurate solution.

Furthermore, we repeated the same analysis for two additional devices. The corresponding device parameters were motivated by experiments carried out by Roth et al. [7, 9] and Bengtsson et al. [12]. Here we found similar results (data not shown), namely that we need at least six or eight basis states to describe Iswap and Cz operations, with similar gate durations.

The results we obtained for the Iswap and Cz gates indicate that the influence of the higher levels $\{|\phi^{m>2}\rangle\}$ on the subspace $\{|\phi^{m\leq 2}\rangle\}$ is not negligible when it comes to modelling these operations. It seems to be the case that higher levels are instrumental in providing enough interaction strength, between the different subsystems, so that we can actually implement the operations (see Figs. 11(a-b) and Figs. 12(a-b) in particular). Additionally, we can observe the trend that larger amplitudes seem to require more basis states N_m. Of course, all previous statements have to be restricted to the specific circuit Hamiltonian we studied here.

b. Architecture II

The second system we consider is defined by means of the circuit Hamiltonian Eq. (8) and the parameters listed in Table II. Here we use a unimodal pulse (we set

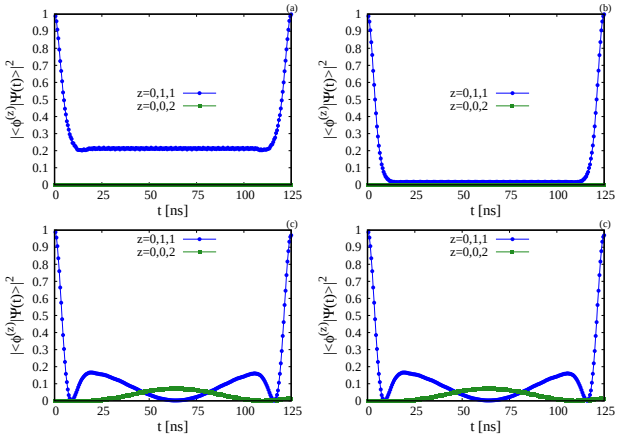

FIG. 14. (Color online) Probabilities $p^{(0,1,1)}(t)$ and $p^{(0,0,2)}(t)$ as functions of time t. We use $N_m = 3$ (a), $N_m = 4$ (b), $N_m = 16$ (c) and $N_m = 25$ (d) basis states to model the system. We use a control pulse of the form Eq. (23), with the pulse parameters $\omega^{\rm D} = 0$ GHz, $T_{\rm r/f} = 20$ ns and $\delta/2\pi = 0.3335$. The pulse duration is $T_{\rm d} = 125.00$ ns. The pulse is supposed to perform a Cz gate. The system we simulate is defined by Eq. (8) and Table II. The $z = (0,1,1) \to z = (0,0,2)$ transition can be used to implement Cz operations, see Ref.[5]. Note that solutions in panel (a) and (b) do not have much in common with the reference solutions in panels (c) and (d).

$\omega^D = 0$) of the form Eq. (23) to implement two-qubit operations. Note that we apply the control pulse to the second flux-tunable transmon (see Table II row $i = 1$).

Figures 13(a-d) show the time evolution of $p^{(0,0,1)}(t)$ and $p^{(0,1,0)}(t)$ as functions of time t, for four different numbers of basis states $N_m = 3$ (a), $N_m = 4$ (b), $N_m = 14$ (c) and $N_m = 25$ (d). We model a transition of the Iswap type.

Obviously, Figs. 13(a,b) have not much in common with the reference solutions (c)/(d). This means that if we use three or four states to model the system, we are not able to implement an Iswap gate on this architecture. We need about fourteen states to model this operation adequately. Additionally, note that during the time evolution $p^{(0,1,0)}(t) + p^{(0,0,1)}(t) \neq 1$ for various times t. The reason for this is that continuous population transfer takes place in the instantaneous basis.

The last case we study is the Cz gate, implemented on architecture II. Figures 14(a-d) show the time evolution of the probabilities $p^{(0,1,1)}(t)$ and $p^{(0,0,2)}(t)$ as functions of time t, for $N_m = 3$ (a), $N_m = 4$ (b), $N_m = 16$ (c) and $N_m = 25$ (d).

In this case we implemented a slightly imperfect Cz operation, i.e., we implemented a pulse which ensures that $p^{(0,1,1)}(T_{\rm d}) < 1$. A perfect Cz gate would only change the relative phase of the state vector but not the population. Therefore, modelling the system with three basis states would yield the same result as modelling the system with 25 states (see Fig. 14(a)), i.e., it does not matter whether or not population exchange actually occurs. However, we want to determine the number of basis states which are needed to model the transitions $z = (0,1,1) \to (0,0,2)$ and $z = (0,0,2) \to (0,1,1)$. The easiest way to do this is to implement a slightly imperfect transition.

Appendix B: Series expansion of the qubit frequency and anharmonicity

We discuss a series expansion for the qubit frequency and anharmonicity which was derived by Didier et al. [22]. The three lowest energy eigenvalues of Hamiltonian Eq. (2) are often approximated by the qubit frequency Eq. (16) and a constant anharmonicity α. In Sec. IV A we show that this approximation is not very accurate in describing the spectrum of Hamiltonian Eq. (16) for various flux control pulses $\varphi(t)$. However, it is possible to make use of alternative expressions which allow us to approximate the spectrum with more precision. Two such expressions were given by Didier et al. [22]. The corresponding flux-tunable transmon qubit frequency is of the form

$$\tilde{\omega}(\varphi) = \sqrt{2E_C E_{J_{\rm eff}}(\varphi)} - \frac{E_C}{4}\sum_{n=0}^{24} a_n \xi(\varphi)^n. \tag{B1}$$

Similarly, the flux-dependent qubit anharmonicity can be expressed as

$$\tilde{\alpha}(\varphi) = -\frac{E_C}{4}\sum_{n=0}^{24} b_n \xi(\varphi)^n, \tag{B2}$$

where a_n and b_n are real coefficients and the function $\xi(\varphi)$ can be expressed as

$$\xi(\varphi) = \sqrt{\frac{E_C}{2E_{J_{\rm eff}}(\varphi)}}. \tag{B3}$$

Note that a_n and b_n can be of order 10^6. Furthermore, for some system parameters (we found this to be the case for a system with an asymmetry factor $d = 0$) we find that $\xi(\varphi) \to 1$ if $\varphi \to \pi/2$. In such cases the approximation can break down. This approximation is also discussed in the main text, see Sec. IV A.

[1] L. D. Landau and E. M. Lifshitz, *Electrodynamics of Continuous Media* (Pergamon, New York, 1984).

[2] A. Agarwal and J. H. Lang, *Foundations of analog and digital electronic circuits* (Elsevier, 2005).

[3] M. H. Devoret, in *Fluctuations quantiques : Les Houches, Session LXIII*, edited by S. Reynaud, E. Giacobino, and J. Zinn-Justin (Elsevier, 1997) pp. 351–386.

[4] M. Ganzhorn, G. Salis, D. J. Egger, A. Fuhrer, M. Mergenthaler, C. Müller, P. Müller, S. Paredes, M. Pechal, M. Werninghaus, and S. Filipp, Phys. Rev. Research **2**, 033447 (2020).

[5] N. Lacroix, C. Hellings, C. K. Andersen, A. Di Paolo, A. Remm, S. Lazar, S. Krinner, G. J. Norris, M. Gabureac, J. Heinsoo, A. Blais, C. Eichler, and A. Wallraff, PRX Quantum **1**, 110304 (2020).

[6] A. Blais, A. L. Grimsmo, S. M. Girvin, and A. Wallraff, Rev. Mod. Phys. **93**, 025005 (2021).

[7] M. Roth, *Analysis of scalable coupling schemes for superconducting quantum computers*, Ph.D. thesis, RWTH Aachen University (2019).

[8] D. C. McKay, S. Filipp, A. Mezzacapo, E. Magesan, J. M. Chow, and J. M. Gambetta, Phys. Rev. Applied **6**, 064007 (2016).

[9] M. Roth, M. Ganzhorn, N. Moll, S. Filipp, G. Salis, and S. Schmidt, Phys. Rev. A **96**, 062323 (2017).

[10] J. Koch, T. M. Yu, J. Gambetta, A. A. Houck, D. I. Schuster, J. Majer, A. Blais, M. H. Devoret, S. M. Girvin, and R. J. Schoelkopf, Phys. Rev. A **76**, 042319 (2007).

[11] X. You, J. A. Sauls, and J. Koch, Phys. Rev. B **99**, 174512 (2019).

[12] A. Bengtsson, P. Vikstål, C. Warren, M. Svensson, X. Gu, A. F. Kockum, P. Krantz, C. Križan, D. Shiri, I.-M. Svensson, G. Tancredi, G. Johansson, P. Delsing, G. Ferrini, and J. Bylander, Phys. Rev. Applied **14**, 034010 (2020).

[13] S. Krinner, S. Lazar, A. Remm, C. Andersen, N. Lacroix, G. Norris, C. Hellings, M. Gabureac, C. Eichler, and A. Wallraff, Phys. Rev. Applied **14**, 024042 (2020).

[14] F. Yan, P. Krantz, Y. Sung, M. Kjaergaard, D. L. Campbell, T. P. Orlando, S. Gustavsson, and W. D. Oliver, Phys. Rev. Applied **10**, 054062 (2018).

[15] C. J. M. DiCarlo, L., B. L. S. Gambetta, J. M., S. D. I. Johnson, B. R., B. A. Majer, J., G. S. M. Frunzio, L., and R. J. Schoelkopf, Nature **460**, 120502 (2019).

[16] H. De Raedt, Comput. Phys. Rep. **7**, 1 (1987).

[17] J. Huyghebaert and H. De Raedt, J. Phys. A: Math. Gen. **23**, 5777 (1990).

[18] M. A. Rol, F. Battistel, F. K. Malinowski, C. C. Bultink, B. M. Tarasinski, R. Vollmer, N. Haider, N. Muthusubramanian, A. Bruno, B. M. Terhal, and L. DiCarlo, Phys. Rev. Lett. **123**, 120502 (2019).

[19] B. Foxen, C. Neill, A. Dunsworth, P. Roushan, B. Chiaro, A. Megrant, J. Kelly, Z. Chen, K. Satzinger, R. Barends, F. Arute, K. Arya, R. Babbush, D. Bacon, J. C. Bardin, S. Boixo, D. Buell, B. Burkett, Y. Chen, R. Collins, E. Farhi, A. Fowler, C. Gidney, M. Giustina, R. Graff, M. Harrigan, T. Huang, S. V. Isakov, E. Jeffrey, Z. Jiang, D. Kafri, K. Kechedzhi, P. Klimov, A. Korotkov, F. Kostritsa, D. Landhuis, E. Lucero, J. McClean, M. McEwen, X. Mi, M. Mohseni, J. Y. Mutus, O. Naaman, M. Neeley, M. Niu, A. Petukhov, C. Quintana, N. Rubin, D. Sank, V. Smelyanskiy, A. Vainsencher, T. C. White, Z. Yao, P. Yeh, A. Zalcman, H. Neven, and J. M. Martinis (Google AI Quantum), Phys. Rev. Lett. **125**, 120504 (2020).

[20] S. Weinberg, *Lectures on Quantum Mechanics*, 2nd ed. (Cambridge University Press, 2015).

[21] M. H. S. Amin, Phys. Rev. Lett. **102**, 220401 (2009).

[22] N. Didier, E. A. Sete, M. P. da Silva, and C. Rigetti, Phys. Rev. A **97**, 022330 (2018).

[23] D. Willsch, *Supercomputer simulations of transmon quantum computers*, Ph.D. thesis, RWTH Aachen University (2020).

[24] H. Lagemann, JUelich Superconducting QUantum Computer Emulator - JUSQUACE, software available from `https://jugit.fz-juelich.de/qip/jusquace` (2020).

[25] D. Willsch, M. Nocon, F. Jin, H. De Raedt, and K. Michielsen, Phys. Rev. A **96**, 062302 (2017).

[26] Jülich Supercomputing Centre, Journal of large-scale research facilities **5**, A135 (2019).

[27] N. V. Vitanov, T. Halfmann, B. W. Shore, and K. Bergmann, Annual Review of Physical Chemistry **52** (2001).